

## Enhancing Cosmological Constraints by Two-dimensional $\beta$ -cosmic-web Weighted Angular Correlation Functions

Fenfen Yin<sup>1,2</sup>, Liang Xiao<sup>2</sup>, Wenying Du<sup>2</sup>, Zhujun Jiang<sup>2</sup>, Zhiwei Min<sup>2</sup>, Jaime Forero-Romero<sup>3</sup>,  
Jiacheng Ding<sup>4</sup>, Le Zhang<sup>2,5,6</sup> and Xiao-Dong Li<sup>2,5,6</sup>

<sup>1</sup> Department of Physics and Electronic Engineering, Tongren University, Tongren 554300, China

<sup>2</sup> School of Physics and Astronomy, Sun Yat-Sen University, Zhuhai 519082, China;  
*zhangle7@mail.sysu.edu.cn; lixiaod25@mail.sysu.edu.cn*

<sup>3</sup> Departamento de Física, Universidad de los Andes, Cra. 1 No. 18A-10 Edificio Ip, CP 111711, Bogotá,  
Colombia; *je.forero@uniandes.edu.co*

<sup>4</sup> Shanghai Astronomical Observatory, Chinese Academy of Sciences, No. 80 Nandan Road, Shanghai  
200030, China; *dingjch@shao.ac.cn*

<sup>5</sup> Peng Cheng Laboratory, No. 2, Xingke 1st Street, Shenzhen 518000, China

<sup>6</sup> CSST Science Center for the Guangdong–Hong Kong–Macau Greater Bay Area, SYSU, Zhuhai 519082,  
China

Received 20xx month day; accepted 20xx month day

**Abstract** We investigate the potential of  $\beta$ -cosmic-web weighted angular correlation functions to improve the cosmological constraints. Using SDSS DR12 CMASS-NGC galaxies and simulated mock catalogs with  $\Omega_m$  varying in the range of 0.25-0.40, we quantify the discriminative power of different statistics via  $\Delta\chi^2$  measurements. Our results demonstrate significant improvements when incorporating weighted statistics. Especially, adding the  $\bar{D}_{\text{nei}}$ -weighting statistics enhances  $\Delta\chi^2$  by 39%-130%, while adding the  $1/\bar{D}_{\text{nei}}$ -weighted statistics yields 229%-336% gains over solely using the traditional angular statistics. These findings align with 3D correlation function studies Yin et al. (2024), confirming the superior performance of  $\beta$ -cosmic-web weighted statistics. The thin-redshift-slice approach makes our method particularly relevant for slitless surveys (such as Euclid, CSST) where redshift errors challenge

traditional 3D analyses. This work also establishes the first theoretical framework for marked statistics in 2D angular clustering.

**Key words:** Cosmology: cosmological parameters – large-scale structure of Universe;  
Methods: statistical

## 1 INTRODUCTION

The cosmic structure originated from early tiny density perturbations. Under the combined influence of gravity and accelerated expansion driven by dark energy, these perturbations gradually give rise to the observed complex and significantly nonlinear structure, which exhibits a wide variety of morphologies and properties at different scales.

The spatial distribution of matter in the universe manifests as a complex, hierarchical network structure termed the “cosmic web”. This anisotropic pattern emerges from gravitational collapse processes dominated by dark matter dynamics, and has constituted a major focus of cosmological research since its first identification in the late 20th century (Bardeen et al. 1986; de Lapparent et al. 1986; Huchra et al. 2012; Tegmark et al. 2004; Guzzo et al. 2014; Suárez-Pérez et al. 2021a; Bond et al. 1996).

The study of the cosmic web relies on large-scale galaxy surveys. Currently, several large-scale survey projects have been successfully implemented, such as the Sloan Digital Sky Survey (SDSS)(York et al. 2000; Abazajian et al. 2003, 2004; Eisenstein et al. 2005; Gott et al. 2005; Adelman-McCarthy et al. 2006; Percival et al. 2007; Adelman-McCarthy et al. 2008; Anderson et al. 2012; Sánchez et al. 2012, 2013; Anderson et al. 2014; Ross et al. 2015; Beutler et al. 2017; Sánchez et al. 2017; Alam et al. 2017; Chuang et al. 2017), the 2-degree Field Galaxy Redshift Survey(2dFGRS)(Colless et al. 2001), the 6-degree Field Galaxy Redshift Survey(6dFGRS)(Beutler et al. 2012, 2011) and the WiggleZ Dark Energy Survey(Parkinson et al. 2012), providing valuable data support for unveiling the mysteries of the cosmic web.

Researchers have invented various methods to describe and analyze the cosmic web. The most popular techniques for describing the cosmic web include the density-based classification (Klypin & Holtzman 1997; Springel et al. 2001; Knollmann & Knebe 2009), T-web (Hahn et al. 2007; Suárez-Pérez et al. 2021b; Forero-Romero et al. 2009), V-web (Hoffman et al. 2012; Forero-Romero et al. 2014), DisPerSE(Sousbie 2011), skeleton algorithms defined based on Lagrangian fluid dynamics (Feldbrugge et al. 2018), and so on. These tools explore the properties of the cosmic web by analyzing the velocity field, density field, or the intuitive geometric distribution of the cosmic web.

---

★ E-mail:

Among the various cosmic web descriptions, the  $\beta$ -skeleton method (Fang et al. 2019; Suárez-Pérez et al. 2021b) utilizes an algorithm originates from the fields of computational geometry and geometric graph theory to describe the properties of the cosmic web. This algorithm constructs a graph to describe the *connectivity* properties from a set of  $n$ -dimensional spatial points, and has been applied in a variety of fields such as machine learning, visual perception, image analysis and pattern recognition (Edelsbrunner et al. 1983; Amenta et al. 1998; Zhang & King 2002). Fang et al. (2019) firstly applied this algorithm to the large-scale structure of the Universe, demonstrating that the cosmic web can be intuitively reconstructed from galaxy spatial distributions, enabling effective visualization of this fundamental structure. García-Alvarado et al. (2020) explored  $\beta$ -cosmic-web and found it reveals significant advantages in characterizing sparsely distributed galaxies. Based on the cosmic web, they further proposed a measure of entropy for describing the complexity of large-scale structures, and built up the relationship between the  $\beta$ -cosmic-web and the traditional T-Web via machine learning methods. Recently, Yin et al. (2024) points out that the environmental information of  $\beta$ -cosmic-web weighting schemes can be utilized to build up mark weighted correlation functions, which can substantially improve the accuracy of the constraints on the cosmological parameters compared to the traditional two-point correlation function.

In the next decade, stage-IV surveys such as Dark Energy Spectroscopic Instrument(DESI)(DESI Collaboration et al. 2016, 2022; Adame et al. 2025), Large Synoptic Survey Telescope(LSST)(LSST Science Collaboration et al. 2009; Ivezić et al. 2019; Crenshaw et al. 2025; Kumar et al. 2025), Euclid Space Telescope(Laureijs et al. 2011; Euclid Collaboration et al. 2022, 2024a; Cuillandre et al. 2024; Euclid Collaboration et al. 2024b,c), and China Space Station Telescope(CSST)(Zhan 2011; Cao et al. 2018; Gong et al. 2019; Zhan 2021; Fu et al. 2023; Luo et al. 2024; Sui et al. 2025; Shi et al. 2025) will provide deep, wide-field observations in much wider range of redshift, producing unprecedented datasets for cosmic web studies. While these surveys provide abundant data for studying the cosmic evolution, the analysis of the data faces new challenges. The stage-IV surveys will unveil complex nonlinear structures, which require more advanced analysis methods. Moreover, some stage-IV surveys (e.g. CSST and Euclid) employ slitless grating spectrometer, which efficiently expand the survey volume/depth but at the cost of reduced redshift measurement precision. This trade-off may significantly impacts data analysis(Gong et al. 2019; Xiao et al. 2023; Gu et al. 2024; Euclid Collaboration et al. 2025b), so we need to adjust the methodology accordingly to address the associated difficulties and limitations brought by the redshift uncertainty.

One possible way to avoid the difficulties brought by redshift uncertainty is to use the two-point angular correlation function (2PACF)(Connolly et al. 2002; Wang et al. 2013; Carvalho et al. 2016; Alcaniz+etal+ et al. 2016; de Carvalho et al. 2018; Carvalho et al. 2020; Venville et al. 2024; Franco et al. 2024; Euclid

(Collaboration et al. 2025a; Wu & Xia 2025), which analyzes cosmic large-scale structures without requiring precise redshift information and is ideal for photometric surveys. Yet the limitation of the 2PACF is that it only captures Gaussian features of the density field, becoming increasingly limited as gravitational collapse enhances non-Gaussianity.

In this work, we develop a novel mark weighted statistic by combining  $\beta$ -cosmic-web classification with angular correlation function analysis. This hybrid approach leads to a novel statistics of mark weighted angular correlation function (hereafter MACF), which preserves the ability to probe non-Gaussian features in large-scale structure while minimizing sensitivity to redshift uncertainties. Notice that the mark weighted correlation functions (MCFs) can extract non-Gaussian information by applying galaxy property weights to angular clustering statistics, thus provides a more complete characterization of nonlinear structure properties. This simple but powerful method has been extensively studied in the last decade. (White 2016; Satpathy et al. 2019; Xiao et al. 2022; Yang et al. 2020; Storey-Fisher et al. 2024; Massara et al. 2024; Xu et al. 2025)

The paper is organized as follows: In Sec. II, we briefly introduce the datasets used in this analysis. In Sec. III, we detail introduce the methodology of building up  $\beta$ -cosmic-web from the 2D galaxy distribution, as well as the methodology for the related MACFs. The results and findings are presented in Sec. IV. We summarize and conclude in Sec. V.

## 2 DATASETS

We investigate the sensitivity of the mark weighted angular correlation functions (MACFs) with  $\beta$ -cosmic-web weights to cosmological parameters. To do this, we compare the measurements from the SDSS BOSS DR12 data with mocks. The mock simulations are produced using COMoving Lagrangian Acceleration (COLA) fast algorithm (Tassev et al. 2013), and then calibrated using SHAM methods (Ding et al. 2024), so that to accurately reproduce CMASS galaxy statistics. For assessing the power of statistics, we compute covariance matrices from Multidark PATCHY (PerturbAtion Theory Catalog generator of Halo and galaxY distributions) (Kitaura et al. 2016) simulations.

### 2.1 The BOSS CMASS Galaxies

The Baryon Acoustic Oscillation Survey (BOSS) project is a crucial component of SDSS-III (Eisenstein et al. 2011; Bolton et al. 2012; Dawson et al. 2013). Its primary scientific goal is to precisely measure expansion and structure growth history via the BAO measurements from the spatial distribution of luminous red galaxies (LRGs) and quasars (Eisenstein et al. 2001). To do this, redshift information for about 1.5 million cosmic galaxies within a sky area of approximately 10,000 square degrees is accurately measured. These galaxies

are divided into two samples of LOWZ and CMASS. The LOWZ galaxy sample includes mainly brightest red galaxies (LRGs) at  $z \leq 0.4$ , while the CMASS sample targets a population of galaxies at higher redshifts, many of which are also in the category of luminous red galaxies (LRGs).

To explore the statistical properties of MACFs, the data must be projected from the three-dimensional space onto a two-dimensional angular space. For simplicity, in this analysis we only use a sub-dataset of the BOSS DR12 CMASS NGC galaxies lying in the redshift range of  $z \in [0.45, 0.55]$ . The process is done by the following steps:

- Firstly, we divide the galaxy sample data in three-dimensional space into six different redshift intervals, each with a redshift thickness  $\Delta z = 0.05$ . So the redshift intervals are  $z \in [0.45, 0.50], [0.46, 0.51], [0.47, 0.52], [0.48, 0.53], [0.49, 0.54], [0.50, 0.55]$ , respectively.
- Then we project each shell of galaxies onto the central redshift plane. The central redshifts of each shell are  $z_{\text{cen}} = 0.475, 0.485, 0.495, 0.505, 0.515, \text{ and } 0.525$ , respectively.

In this way, we created overlapping bins of galaxies as 2D projections. We allow overlapping of bins, in order to 1) better trace the evolution of clustering patterns across redshift, and 2) minimize the information loss due to the boundary effects between adjacent redshift bins.

## 2.2 COLA Mock Catalogues

COLA (Tassev et al. 2013) is a hybrid simulation method that integrates second-order Lagrangian perturbation theory (2LPT) and N-body algorithms, offering an effective solution for simulating dark matter (DM) particles. The perturbation theory results, which can successfully describe large-scale clustering processes, can replace the time integration calculations of N-body simulations on linear scales, so the large-scale and small-scale evolution processes are decoupled and separately treated. In the large-scale structure evolution, the evolution of dark matter particles can be described by the precise 2LPT theory results to describe their dynamical behaviors, while on small scales the evolution is carried out with well-established N-body simulation methods. To achieve this goal, COLA introduces a co-moving framework to place dark matter particles in a co-moving coordinate system that moves together with the “LPT observer”. Although COLA sacrifices some accuracy on small scales, it can greatly improve computational efficiency by 10-100 times, while the accuracy on relatively large clustering scales is still quite good.

In this paper we used the mock SDSS CMASS galaxy catalogs produced in Ding et al. (2024). The mocks are based on a set of simulation assumes a flat  $\Lambda$ CDM with  $\Omega_m$  varying in region of  $0.29 < \Omega_m < 0.33$ , and the other parameter values fixed  $\Omega_b = 0.048$ ,  $w = -1.0$ ,  $\sigma_8 = 0.82$ ,  $n_s = 0.96$ , and  $h = 0.67$ , which

are close to the average constraints of Planck 2015 results (Planck Collaboration et al. 2016). Each set of COLA simulation uses  $1024^3$  particles in a cubic box with a side length of  $800h^{-1}$  Mpc. Ding et al. (2024) then applied the subhalo abundance matching (SHAM) method to COLA simulations to efficiently generate mock galaxies. Three parameters, including the scatter magnitude  $\sigma_{\text{scat}}$  in SHAM, the initial redshift of the COLA simulations  $z_{\text{init}}$  and the time step  $da$ , are tested to achieve a good match. A good agreement between COLA-simulated galaxies and CMASS NGC galaxies is achieved on scales ranging from 4 to  $20 h^{-1}$  Mpc by setting  $z_{\text{init}} = 29$  and  $da = 1/30$ . Finally, by comparing various statistical properties such as anisotropic 2PCF, three-point clustering, and power spectrum multipoles, the authors found their COLA mocks achieve equally good performance when compared to GADGET mocks (in the region of  $s \geq 4h^{-1}$  Mpc and  $k \leq 0.3h\text{Mpc}^{-1}$ ), while the computational cost is two orders of magnitude lower than the latter one.

Following the methodology of Yin et al. (2024), in this proof-of-concept analysis we only used three sets of mock simulations with  $\Omega_m = 0.25, 0.31, 0.4$  to assess the constraining power of the statistics. Following the same procedure applied to observational data, we process each simulation by dividing them into six overlapping redshift bins and projecting onto 2D angular planes. For illustration purpose, Figure 1 compares the 2D positions of the observational and mock galaxies, in the  $z \in [0.48, 0.53]$  subsample. This figure reveals very good similarity in angular galaxy distributions between COLA simulations and CMASS-NGC observations.

### 2.3 PATCHY Mocks

The PATCHY mock catalogs (Kitaura et al. 2016) combine efficient structure formation models with local, nonlinear, and scale-dependent stochastic biasing to generate realistic dark matter halo distributions. These mocks are constructed using augmented Lagrangian perturbation theory (2LPT for large scales plus spherical collapse for small scales), which evolves Gaussian density fluctuations into a full dark matter density field while self-consistently calculating peculiar velocities. The catalogs are carefully calibrated against the high-precision BigMultiDark N-body simulation( Kitaura et al. 2014; Rodríguez-Torres et al. 2016) (contains  $3840^3$  particles in a volume of  $(2.5h^{-1}\text{Gpc})^3$  with  $\Lambda\text{CDM}$  parameters:  $\Omega_m = 0.307, \Omega_b = 0.048, \sigma_8 = 0.82, n_s = 0.96, h = 0.67$ ) through an analytic statistical biasing models.

For our analysis, we project the 3D PATCHY simulations into six distinct 2D shell layers matching the CMASS-NGC observational slices. To save the computational cost, we only used the first 300 realizations from the total 2,048 PATCHY mock realizations, which are enough for this simple proof-of-concept work. These mocks are used to compute the covariance matrices for the  $\beta$ -cosmic-web weighted angular correlation functions (MACF).

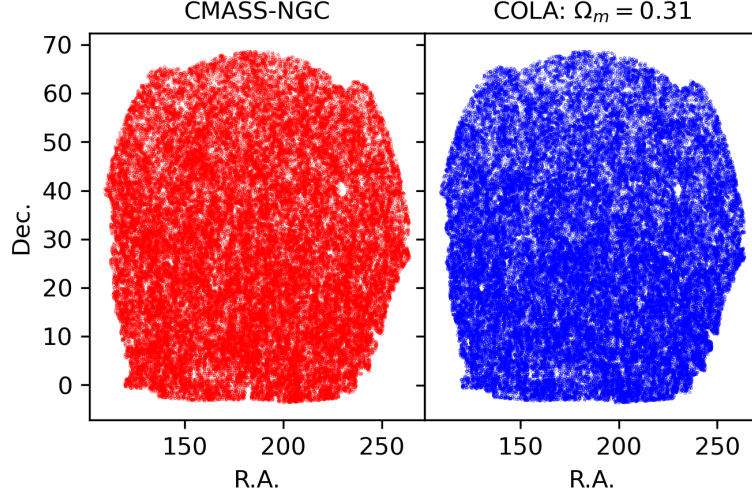


Fig. 1: A comparison of the R.A.-Dec. distribution of the CMASS-NGC galaxies (left panel) and galaxies in the  $\Omega_m = 0.31$  COLA mock (right panel). The 2D shell datasets are derived from the 3D samples within the redshift interval  $z \in [0.48, 0.53]$ , projected onto the central redshift plane  $z_{\text{cen}} = 0.505$ . We find good consistency between the angular distributions of simulated and observed galaxies, validating our simulation framework.

### 3 METHODOLOGY

In this section we will introduce our methodology. We begin by detailing the theoretical foundations and construction methodology of  $\beta$ -skeletons. Then we will introduce our novel mark weighted correlation function statistics.

#### 3.1 Two-dimensional $\beta$ -cosmic-web

The  $\beta$ -skeleton algorithm originates from the fields of computational geometry and geometric graph theory. It is similar to the minimum spanning tree (MST) algorithm (Barrow et al. 1985), with a key distinction being that the structural graph constructed relies on  $\beta$ -parameter, which makes it flexible in handling point sets with complex neighbor relationships (Kirkpatrick & Radke 1985; Correa & Lindstrom 2013).

The definition of  $\beta$ -skeleton is as follows. For a point set  $S$  in  $n$ -dimensional Euclidean space, any two points  $p$  and  $q$  in the point set  $S$  are considered connected if there is no third point in the *empty regions*, which is illustrated in the Figure 2<sup>1</sup>:

<sup>1</sup> The  $\beta$ -skeleton code utilized in this paper can be accessed at the following link: <https://github.com/xiaodongli1986/LSSCode>

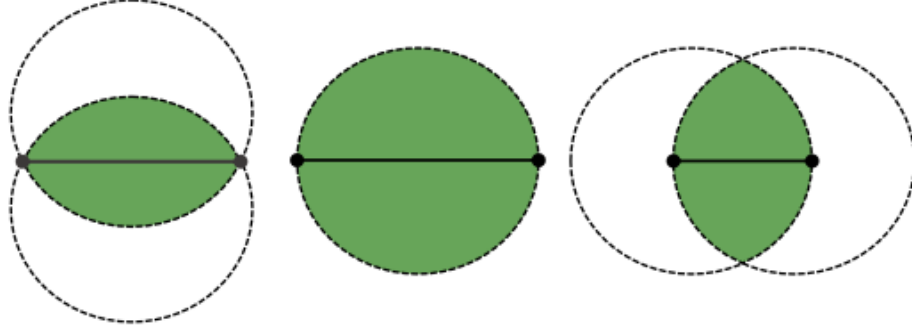


Fig. 2: Lune-based definition of the empty regions of the  $\beta$ -skeleton. Left:  $\beta < 1$ , Center:  $\beta = 1$ , Right:  $\beta > 1$ .

- For  $0 < \beta < 1$ , the empty region is formed by the intersection of two spheres with diameter  $d_{pq}/\beta$ , having  $p$  and  $q$  on their boundaries, where  $d_{pq}$  is the common chord of the spheres.
- For  $\beta = 1$ , the empty region becomes a sphere with diameter  $d_{pq}$ .
- For  $\beta > 1$ , there are two different definitions of the empty region: the Circle-based definition and Lune-based definition. In this paper we adopt the Lune-based definition, i.e. the empty region is the intersections of two spheres with a diameter of  $\beta d_{pq}$  and their centers locating at  $p + \beta(q - p)/2$  and  $q + \beta(p - q)/2$ , respectively.

The  $\beta$ -skeleton defined in this way exhibits a series of unique and interesting mathematical properties:

- Hierarchical nature. As  $\beta$  varies from 0 to  $\infty$ , the constructed  $\beta$ -skeleton graph transitions from a complete graph to an empty graph. In particular, the graphs formed by the special case of  $\beta = 1$  is called Gabriel Graph, which is known to contain the Euclidean minimum spanning tree, while in image analysis the  $\beta = 1.7$  *Circle-based* graphs are found to accurately reconstruct the entire boundary of any smooth surface, without generating any edges that do not belong to the boundary, as long as the samples are sufficiently dense with respect to the local curvature of the surface.
- Inclusion relation. For any parameter value satisfying  $\beta_1 < \beta_2$ , for fixed points  $p$  and  $q$ , the empty region of the  $\beta$ -skeleton with  $\beta_2$  contains the empty region of the  $\beta$ -skeleton with  $\beta_1$  as the set parameter value. This property ensures that the connectivity of the web gradually decreases as increasing  $\beta$ .
- Parametric control. The parameter  $\beta$  provides an intuitive and powerful “sparse-dense” adjustment knob allowing researchers to finely tune the web’s connection pattern according to the specific needs of scientific research, so that to conveniently visualize the web structures of the set.



- Interpret-ability.  $\beta$ -skeleton is directly based on the geometric distribution of matter, which makes the results of the model highly intuitive and understandable.

In Figure 3, we visualize 2D  $\beta$ -cosmic-web for CMASS-NGC galaxy data using  $\beta = 1$ ,  $\beta = 3$ , and  $\beta = 5$ . The datasets chosen as galaxies within the redshift interval  $[0.48, 0.53]$ . For visualization purpose, we only plot 1500 galaxies with R.A.  $\in [220^\circ, 230^\circ]$  and Dec.  $\in [30^\circ, 45^\circ]$ , corresponds to a  $236.08h^{-1}\text{Mpc} \times 354.12h^{-1}\text{Mpc}$  slice, respectively. We find that  $\beta = 1$  leads to a network which exhibits dense connections, while for  $\beta = 5$  the connections become notably sparse. Specifically,

- $\beta = 1$  web has 2695 links (overconnected). It contains a substantial number of extraneous and unnecessary galaxy connections that do not reflect true connection patterns.
- $\beta = 3$  yields 1467 connections (nearly 1:1 with the number of galaxies) and is considered to properly reflect the connection relationships among galaxies more realistically.
- $\beta = 5$  reduces to 1150 links (relatively sparse), omitting rich structural details.

Following Yin et al. (2024), we adopt the  $\beta = 3$  web as the foundation for our analysis, as its topological structure is close to most people’s conceptual understanding of the cosmic web.

The  $\beta = 3$  webs constructed from CMASS-NGC and COLA simulations with different  $\Omega_m$  ( $\Omega_m = 0.31$ ,  $\Omega_m = 0.25$ ,  $\Omega_m = 0.4$ ) are illustrated in Figure 4. Similar to Figure 3, we only plot galaxies with  $z \in [0.48, 0.53]$ , R.A.  $\in [220^\circ, 230^\circ]$  and Dec.  $\in [30^\circ, 45^\circ]$ . This figure shows that the results of the  $\Omega_m = 0.31$  mock is statistically most consistent with the observations. In terms of connectivity, we find the web of CMASS-NGC subsample has 1467 connections, while the  $\Omega_m = 0.31$  mock has 1534 connections, which is pretty close. Larger discrepancy is detected for webs constructed using the  $\Omega_m = 0.25$  mock (1548 connections) and the  $\Omega_m = 0.4$  mock (1359 connections).

### 3.2 Mark weighted angular correlation functions (MACFs) using 2D $\beta$ -cosmic-web

We define mark weighted angular correlation functions, utilizing the 2D  $\beta$ -skeleton cosmic web statistics as weighting factors. Following the methodologies developed in Yin et al. (2024), we use three different quantities in the weighting:

- Connection number ( $N_{\text{con}}$ ): the number of neighboring galaxies around each galaxy.
- Mean neighbor distance ( $\bar{D}_{\text{nei}}$ ): the average distance between each galaxy and its neighboring galaxies.
- Inversed neighbor distance ( $1/\bar{D}_{\text{nei}}$ ): the reciprocal of mean neighbor distance.

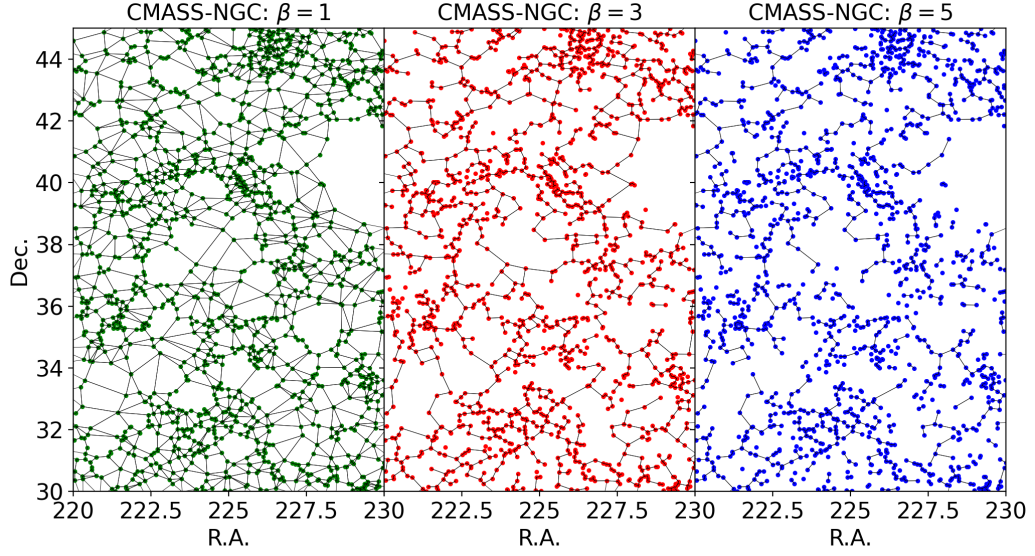


Fig. 3: Visual comparisons of 2D  $\beta$ -cosmic-webs from CMASS-NGC data, with  $\beta$  set to 1, 3 and 5, respectively. The structures are derived from galaxies with  $z \in [0.48, 0.53]$ . Similar to Yin et al. (2024), in what follows we adopt the  $\beta = 3$  results as the foundation for our analysis, as its topological structure is close to our conceptual understanding of the cosmic web.

The weighting scheme can be specifically expressed as follows:

$$\text{wei}(\mathbf{x}) = \begin{cases} N_{\text{con}}(\mathbf{x}), & \text{case I} \\ \bar{D}_{\text{nei}}(\mathbf{x}), & \text{case II} \\ 1/\bar{D}_{\text{nei}}(\mathbf{x}), & \text{case III} \end{cases} \quad (1)$$

Isolated galaxies (no neighbors) are assigned  $w(\mathbf{x}) = 0$ . The reciprocal distance measure  $1/\bar{D}_{\text{nei}}$  in 2D projections tends to amplify extreme values, potentially causing divergence. To ensure numerical stability, we implement a cutoff threshold  $\text{wei}_{\text{cut}}$  (defined as the 95th percentile of  $1/\bar{D}_{\text{nei}}$  distribution). All values exceeding this threshold are truncated at  $\text{wei}_{\text{cut}}$ , effectively controlling outliers while retaining essential nonlinear clustering features.

Figure 5 visualizes 2D  $\beta$ -cosmic-web weights of CMASS-NGC observational galaxies. The weights of galaxies are denoted by the circle sizes. In different weighting schemes, we find different environment-dependence of the weights. In the left panel, the sizes of the circles are not very different from each other, indicating that the dependence of  $N_{\text{con}}(\mathbf{x})$  on the environment is weak. When  $\bar{D}_{\text{nei}}(\mathbf{x})$  is used as weight, it upweights the low-density regions, while its inverse  $1/\bar{D}_{\text{nei}}(\mathbf{x})$  highlights the overdense regions.

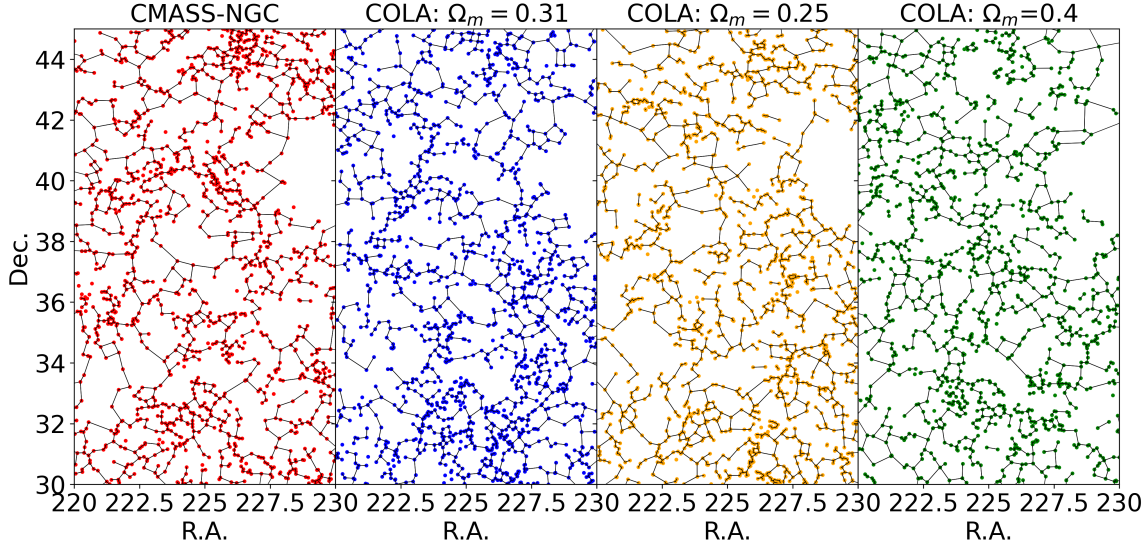


Fig. 4: The  $\beta = 3$  web of the CMASS-NGC galaxies and the COLA mocks with  $\Omega_m = 0.31, 0.25, 0.4$ . In all plots we chose galaxies with  $z \in [0.48, 0.53]$ , R.A.  $\in [226^\circ, 230^\circ]$  and Dec.  $\in [38^\circ, 42^\circ]$ . By comparing the connectivity of these webs, we find COLA simulation with  $\Omega_m = 0.31$  exhibits the strongest agreement with the observational data.

Based on these weights, the mark weighted two-point correlation functions, denoted as  $W(s)$ , are then computed through Landy–Szalay estimator (Landy & Szalay 1993):

$$W(s) = \frac{DD(s) - 2DR(s) + RR(s)}{RR(s)}. \quad (2)$$

Assuming a flat cosmological model, the comoving distance between galaxies at redshifts  $z_1$  and  $z_2$  respectively can be expressed as

$$s = \sqrt{r^2(z_1) + r^2(z_2) - 2r(z_1)r(z_2)\cos\theta} \quad (3)$$

where  $r(z_1), r(z_2)$  represent the comoving distances from the observer for two galaxies at redshifts of  $z_1$  and  $z_2$ , respectively, and  $\theta$  is the angular distance between galaxy pairs. In  $\Lambda$ CDM model, the comoving distance  $r(z)$  of a galaxy with redshift  $z$  takes form of,

$$r(z) = \frac{1}{H_0} \int_0^z \frac{dz'}{\sqrt{\Omega_\Lambda + \Omega_m(1+z')^3}}. \quad (4)$$

In 2D case, for a set of galaxies with the center of redshift bin denoted as  $z_{\text{center}}$ , the angular component of the comoving distance between galaxy pairs take the form of

$$s_\perp = \sqrt{2r^2(z_{\text{center}}) - 2r^2(z_{\text{center}})\cos\theta} = 2r(z_{\text{center}})\sin\left(\frac{\theta}{2}\right), \quad (5)$$

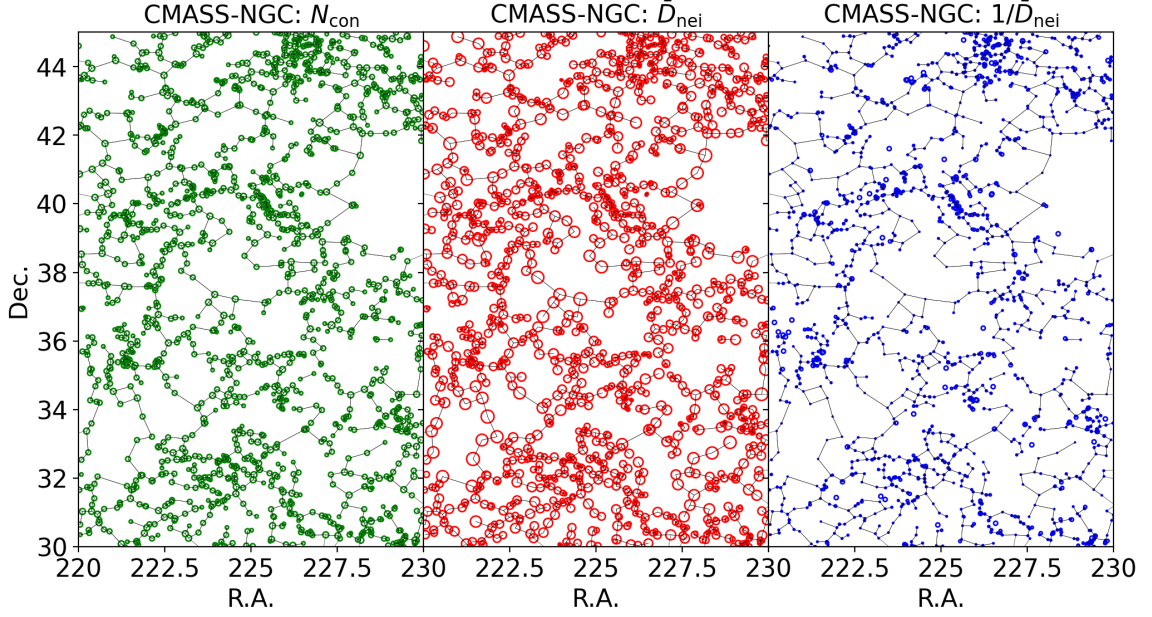


Fig. 5: The 2D  $\beta$ -cosmic-web weights for CMASS-NGC galaxies under  $\beta = 3$  are visualized via circle sizes, covering  $\text{R.A.} \in [220^\circ, 230^\circ]$  and  $\text{Dec.} \in [30^\circ, 45^\circ]$  regions. Derived from a 2D shell formed 3D spatial data with  $\Delta z = 0.05$  and  $z \in [0.48, 0.53]$  projected at  $z_{\text{cen}} = 0.505$ , three weighting schemes are compared: Left ( $N_{\text{con}}$ ): Uniform weighting across different density regions. Middle ( $\bar{D}_{\text{nei}}$ ): Enhanced emphasis on low-density environments. Right ( $1/\bar{D}_{\text{nei}}$ ): Strong prioritization of high-density structures.

where “ $\perp$ ” denotes that this component is perpendicular to the line-of-sight (LOS), and  $\theta$  is the angular separation of the two galaxies. This formula can be used to convert the measurement to the angular correlation function  $w(\theta)$  (Matsubara et al. 2004; Carvalho et al. 2016, 2020), which explicitly depends on  $\theta$  instead of  $s$ . This is equivalent to calculating  $w(\theta)$  directly using the Landy–Szalay estimator (Landy & Szalay 1993),

$$w(\theta) = \frac{DD(\theta) - 2DR(\theta) + RR(\theta)}{RR(\theta)}. \quad (6)$$

In this work we only use the monopole component  $W_0$ . To mitigate the influence of galaxy bias and improve the accuracy of analysis, we further normalize the correlation function, i.e.

$$\hat{w}(\theta) = \hat{W}_0(s) = \frac{W_0(s)}{\int_a^b W_0(s) ds}. \quad (7)$$

We tested the influence of  $a$ ,  $b$ , and chose  $a = 10 h^{-1}\text{Mpc}$  and  $b = 58 h^{-1}\text{Mpc}$  as our baseline values, representing a conservative choice that balances the information and systematics. In the analysis, we split the clustering range into eight bins.

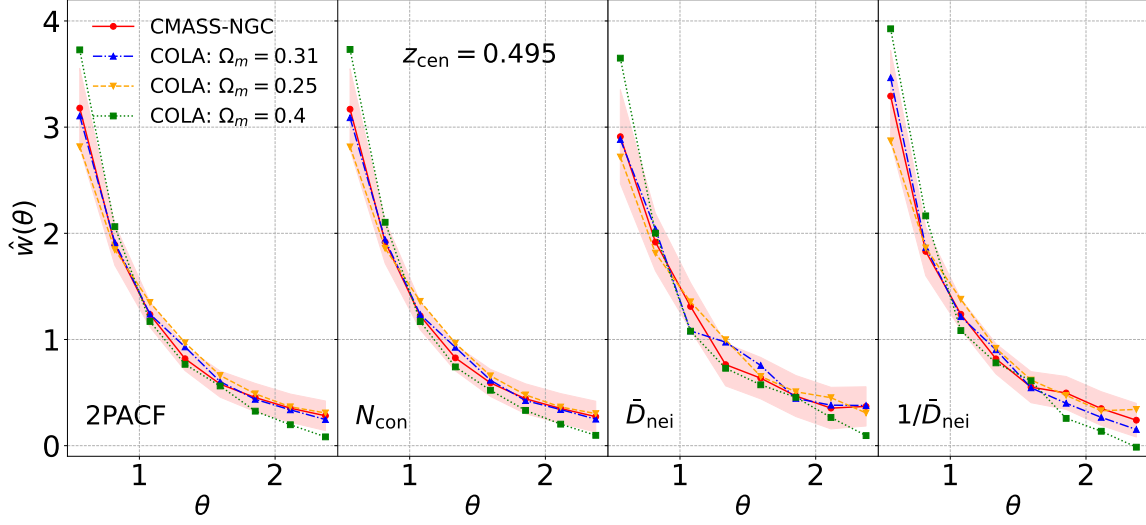


Fig. 6: Comparison of normalized angular correlation functions  $\hat{w}(\theta)$  for CMASS-NGC (red) and COLA simulations with  $\Omega_m = 0.31$  (blue),  $0.25$  (orange),  $0.4$  (green) using galaxies with  $z \in [0.47, 0.52]$ , computed in the range of  $\theta \in [0.45^\circ, 2.52^\circ]$ . The shaded region represents  $3\sigma$  confidence interval. Results of the  $\Omega_m = 0.31$  COLA mock is most consistent with the observational data, while both  $\Omega_m = 0.25$  or  $\Omega_m = 0.4$  exhibits significant discrepancies ( $> 3\sigma$ ) from the deviate from the CMASS-NGC data.

Figure 6 compares the  $\hat{w}(\theta)$ s measured from CMASS-NGC galaxies (red) and COLA mocks with  $\Omega_m = 0.31$  (blue),  $0.25$  (orange),  $0.4$  (green), using galaxies with  $z \in [0.47, 0.52]$ . Measurements from the standard 2PACF and the MACFs weighted by  $N_{\text{con}}$ ,  $\bar{D}_{\text{nei}}$  and  $1/\bar{D}_{\text{nei}}$  are plotted. COLA with  $\Omega_m = 0.31$  aligns with CMASS-NGC within the  $3\sigma$  confidence interval, while  $\Omega_m = 0.25$  or  $\Omega_m = 0.4$  simulations show evident discrepancy from the data. The trend is similar for other redshift intervals (e.g. Figure 7 compares the measurements of galaxies with  $z \in [0.48, 0.53]$ ).

To assess the constraining power of different statistics, we define the  $\chi^2$  as

$$\chi^2 = (\Delta \mathbf{p})^T \cdot \mathbf{C}^{-1} \cdot \Delta \mathbf{p}, \quad (8)$$

where  $\Delta \mathbf{p}$  characterizes the difference between the measurements from the data ( $\mathbf{p}_{\text{data}}$ ) and the COLA mocks ( $\mathbf{p}_{\text{model}}$ )

$$\Delta \mathbf{p} = \mathbf{p}_{\text{model}} - \mathbf{p}_{\text{data}}. \quad (9)$$

The covariance matrix corresponding to the normalized weighted angular correlation function statistic  $\hat{w}(\theta)$  is represented by the symbol  $\mathbf{C}$ . By varying the value of  $\Omega_m$ , the variation of the  $\chi^2$  values can be utilized to evaluate the sensitivity of a specific statistics to the cosmological parameter, thereby enabling us to compare

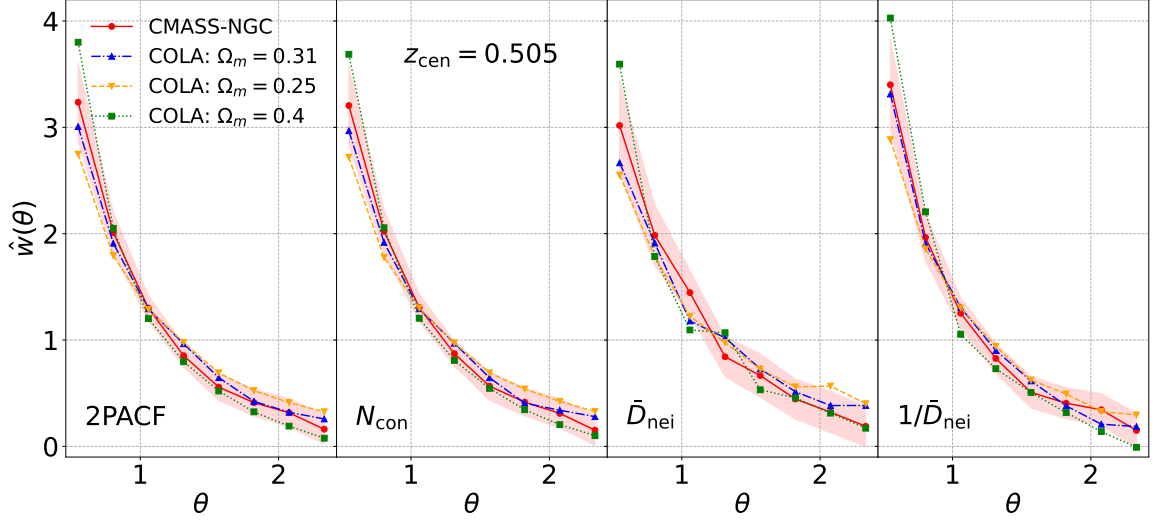


Fig. 7: Similar to Figure 6, but measured in the redshift interval of  $[0.48, 0.53]$ . Still we find  $\Omega = 0.31$  mock best agrees with the results from the observational data.

the power of different statistics. The covariance matrix is computed via

$$C = \langle (\mathbf{p} - \bar{\mathbf{p}}) (\mathbf{p} - \bar{\mathbf{p}})^T \rangle \quad (10)$$

$$= \frac{1}{N_{\text{mock}} - 1} \sum_{i=1}^{N_{\text{mock}}} (\mathbf{p}_i - \bar{\mathbf{p}}) (\mathbf{p}_i - \bar{\mathbf{p}})^T \quad (11)$$

where the vector  $\mathbf{p}_i$  denotes the  $i$ th PATCHY mock among all  $N_{\text{mock}}$  mocks, and  $\bar{\mathbf{p}}$  denotes the average value of  $\mathbf{p}$  over all PATCHY mocks. In this analysis we employed 300 sets of PATCHY simulations to estimate the covariance matrix. This number is large enough considering that our data vector  $\mathbf{p}$  only have 8 components.

To reduce the statistical fluctuation and enhance the robustness of the results, we use the average of the  $\chi^2$ 's in the six subsamples (with different but overlapping redshift ranges) to assess the power of different statistics:

$$\overline{\chi^2} = \frac{1}{n} \sum_{i=1}^n \chi_i^2 \quad (12)$$

where the value of  $n$  is 6, and  $\chi_i^2$  corresponds to the chi-square value calculated for an individual 2D shell of galaxies.

## 4 RESULTS

Figure 8 shows the correlation coefficient of the  $z \in [0.48, 0.53]$  subsample. To precisely quantify the relationships between different statistical measures, the figure displays both the autocorrelation of the correlation

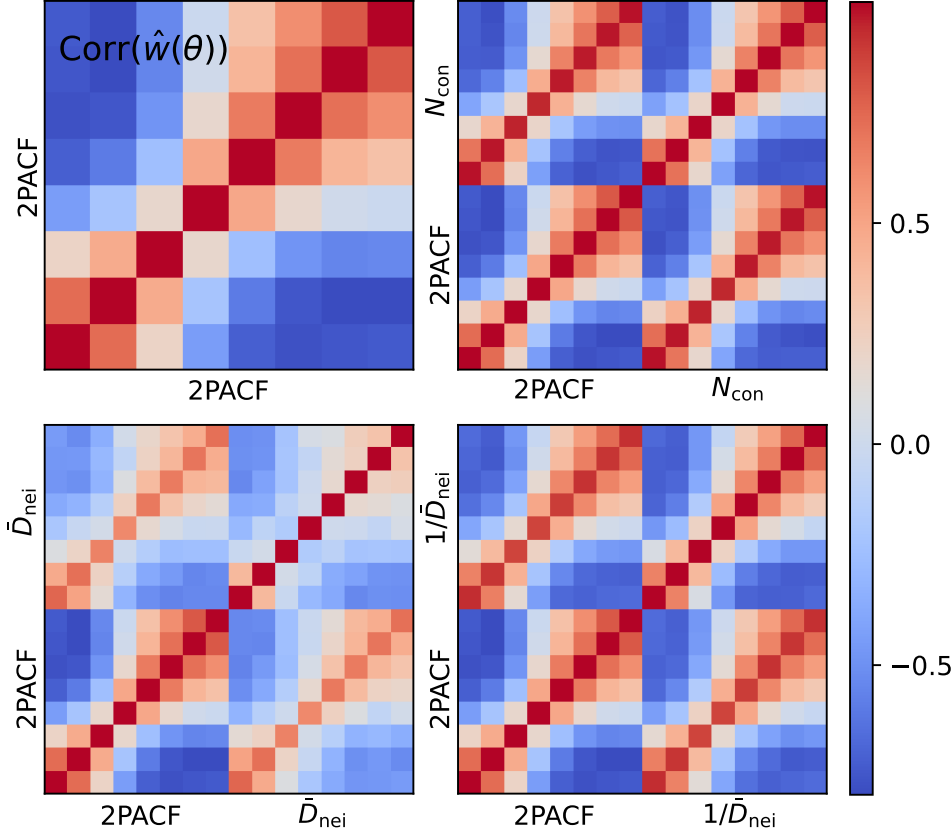


Fig. 8: Correlation coefficients for normalized angular correlation function  $\hat{w}(\theta)$  computed using PATCHY simulations. Here we only showed results of the  $z \in [0.48, 0.53]$  sample.

functions and the cross-correlation coefficients between the standard 2PACF and the  $\hat{w}(\theta)$  weighted by  $N_{\text{con}}$ ,  $\bar{D}_{\text{nei}}$ , and  $1/\bar{D}_{\text{nei}}$ , respectively. Among them, the MACF weighted by  $N_{\text{con}}$  is most correlated with the original 2PACF, since this weighting scheme is most close to uniform weighting.

The sensitivity of  $\hat{w}(\theta)$  to cosmological parameter is then evaluated using

$$\Delta\chi^2 \equiv \chi^2 - \chi_{\min}^2 \quad (13)$$

which directly measures the statistical power to discriminate between different cosmologies. To enhance the stability and robustness of our results, we compute the mean  $\Delta\chi^2$  cross the six overlapping redshift bins, defined as:

$$\overline{\Delta\chi^2} \equiv \overline{\chi^2} - \overline{\chi_{\min}^2} \quad (14)$$

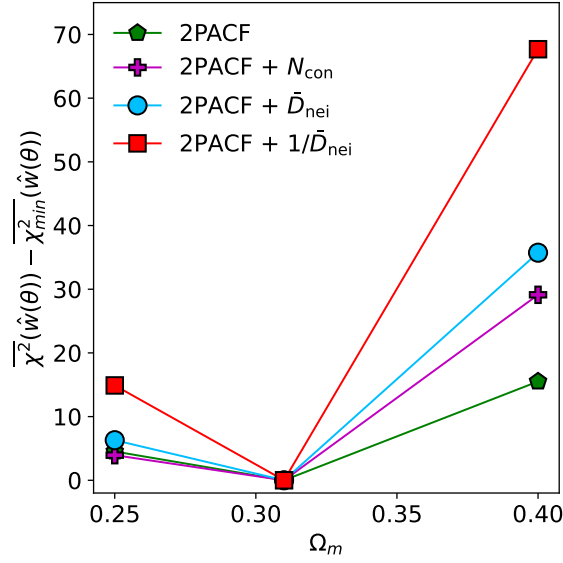


Fig. 9: The variation of  $\Delta\overline{\chi^2}$  as  $\Omega_m$  changes from 0.25 to 0.4. It reveals a minimum  $\overline{\chi^2}_{\min}$  at  $\Omega_m = 0.31$ , distinctively lower than values at other two  $\Omega_m$ . Combination of 2PACF and  $\hat{w}(\theta)$  weighted by  $1/\bar{D}_{\text{nei}}$  (represented by red squares) yields to the highest sensitivity to  $\Omega_m$ .

where  $\overline{\chi^2}$  and  $\overline{\chi^2}_{\min}$  represent the averaged  $\chi^2$  values over all bins. This averaging procedure is aimed to 1) reduce statistical fluctuations due to our relatively small sample size and 2) improve robustness against chance variations in our proof-of-concept analysis (which currently considers only three simulations). By adopting this approach, we effectively mitigate the statistical fluctuations while maintaining the sensitivity of cosmological parameters.

Figure 9 presents the variation of  $\Delta\overline{\chi^2}$  as  $\Omega_m$  varies from 0.25 to 0.4. In all cases we find  $\Omega_m = 0.31$  leads to the minimal  $\chi^2$ , so it always serves as the baseline. We find that:

- The incorporation of weighted statistics provides significant improvement over using the two-point angular correlation function (2PACF) alone, as evidenced by the enhanced  $\Delta\overline{\chi^2}$ . This demonstrates greater statistical power for constraining cosmological parameters.
- Among all tested combinations, the most sensitive probe of  $\Omega_m$  is achieved by combining 2PACF with the  $\hat{w}(\theta)$  statistic weighted by  $1/\bar{D}_{\text{nei}}$  (red squares in Figure 9), enlarging the value of  $\Delta\chi^2$  by 2-3 times.

To quantitatively assess the improvement gained by incorporating  $\beta$ -cosmic-web-weighted  $\hat{w}(\theta)$  statistics compared to the conventional 2PACF approach, we introduce the relative sensitivity metric:

$$r = \frac{\Delta\overline{\chi^2}}{\Delta\overline{\chi^2}_{\text{2PACF}}} - 1. \quad (15)$$



Statistics	$\Delta\chi^2(r)_{(\Omega_m=0.25)}$	$\Delta\chi^2(r)_{(\Omega_m=0.40)}$
2PACF	4.52 (0%)	15.51 (0%)
2PACF+ $\hat{w}(\theta)_{N_{\text{con}}}$	3.94 (-13%)	29.12 (88%)
2PACF+ $\hat{w}(\theta)_{\bar{D}_{\text{nei}}}$	6.30 (39%)	35.73 (130%)
2PACF+ $\hat{w}(\theta)_{1/\bar{D}_{\text{nei}}}$	14.89 (229%)	67.68 (336%)

Table 1: The sensitivity of statistics to  $\Omega_m$ , quantified using  $r$  (Equation 15). The percentage improvements of  $\Delta\chi^2$  (compared with the 2PACF alone results) are shown in the parentheses. The  $1/\bar{D}_{\text{nei}}$ -weighted  $\hat{w}(\theta)$  shows the strongest improvement, improving the value by 229% ( $\Omega_m = 0.25$ ) to 336% ( $\Omega_m = 0.4$ ).

The statistical improvements are summarized in Table 1. Our analysis reveals that combining the two-point angular correlation function (2PACF) with the mark weighted angular correlation function (MACF) significantly enhances the statistical confidence. Specifically:

- Incorporating  $D_{\text{nei}}$ -weighted statistics boosts the  $\Delta\chi^2$  values by 39%–130%, indicating substantially improved parameter constraints.
- The  $1/D_{\text{nei}}$  weighting scheme shows even more dramatic improvement, enhancing  $\Delta\chi^2$  by 229%–336%. Statistically, this enhancement is equivalent to increasing our dataset by the same amount.

## 5 CONCLUDING REMARKS

In this paper, we investigate whether cosmological constraints can be improved using the  $\beta$ -cosmic-web weighted angular correlation functions. We compare the statistical measurements from the SDSS DR12 CMASS-NGC galaxies and the COLA mocks with different values of  $\Omega_m$  (0.25, 0.31 and 0.4), and use different statistics to distinguish between these  $\Lambda$ CDM cosmologies. We quantify the statistical power of each method using the value of  $\Delta\chi^2$ .

Our results show that adding the  $\beta$ -cosmic-web weighted statistics can effectively enhance the statistical power. Specifically, the  $D_{\text{nei}}$ -weighted statistics boosts the  $\Delta\chi^2$  values by 39%–130%, while the  $1/D_{\text{nei}}$  weighting scheme shows even more dramatic improvement, enhancing  $\Delta\chi^2$  by 229%–336%.

The procedure of this analysis is similar to Yin et al. (2024), where the authors investigated the statistical power of  $\beta$ -cosmic-web weighted correlation functions, and found  $\approx 100\%$ – $800\%$  enhancement in  $\Delta\chi^2$  when adding one weighted statistic into the analysis (they found adding more than one weighted statistic can improve the  $\Delta\chi^2$  by 928%). In this paper we investigate the 2D angular statistics, and also found significant enhancement of constraining power. Notably, both studies show the  $1/\bar{D}_{\text{nei}}$  weighting scheme performs

best, suggesting dense regions contain substantial cosmological information, while the  $N_{\text{con}}$  weighting provides minimal improvement. While in this paper we only focus on the constraints of  $\Omega_m$ , it is expected that this statistic is also sensitive to other physics such as dark energy.(Riess et al. 1998; Perlmutter et al. 1999; Weinberg 1989; Li et al. 2011; Yoo & Watanabe 2012; Weinberg et al. 2013)

The statistics developed in this paper are defined based on thin redshift slices, making them potentially applicable to slitless surveys such as Euclid and CSST, where redshift errors may significantly impact traditional 3D clustering analyses. Considering that no previous work has discussed marked statistics using 2D angular clustering, this study also provides value from a purely theoretical perspective.

In this proof-of-concept paper, we only considered three weighting schemes. Since the dependence of clustering on the environment is complex and varied, we expect cosmological constraints could be further enhanced by exploring additional weighting approaches (such as  $\rho^\alpha$ ,  $(|\nabla\rho|/\rho)^\alpha$ , and others). Furthermore, to better prepare for slitless survey analyses, machine learning algorithms and scattering transforms on 2D redshift-sliced data also warrant investigation. We will explore these directions in future works.

## 6 ACKNOWLEDGMENTS

This work is supported by the Ministry of Science and Technology of China (2020SKA0110401, 2020SKA0110402, 2020SKA0110100), the National Key Research and Development Program of China (2018YFA0404504, 2018YFA0404601, 2020YFC2201600), the National Natural Science Foundation of China (12373005, 11890691, 12205388, 12220101003, 12473097), the China Manned Space Project with numbers CMS-CSST-2021 (A02, A03, B01), Guangdong Basic and Applied Basic Research Foundation (2024A1515012309). This work was performed using the Tianhe-2 supercomputer and the Kunlun cluster in the School of Physics and Astronomy at Sun Yat-Sen University. We also wish to acknowledge the Beijing Super Cloud Center (BSCC) and Beijing Beilong Super Cloud Computing Co., Ltd (<http://www.blsc.cn/>) for providing HPC resources that have significantly contributed to the research results presented in this paper.

## References

- Abazajian, K., Adelman-McCarthy, J. K., Agüeros, M. A., et al. 2003, AJ, 126, 2081 2
- Abazajian, K., Adelman-McCarthy, J. K., Agüeros, M. A., et al. 2004, AJ, 128, 502 2
- Adame, A. G., Aguilar, J., Ahlen, S., et al. 2025, JCAP, 2025, 021 3
- Adelman-McCarthy, J. K., Agüeros, M. A., Allam, S. S., et al. 2006, ApJS, 162, 38 2
- Adelman-McCarthy, J. K., Agüeros, M. A., Allam, S. S., et al. 2008, ApJS, 175, 297 2
- Alam, S., Ata, M., Bailey, S., et al. 2017, MNRAS, 470, 2617 2

- Alcaniz+etal+, J. S., Carvalho, G. C., Bernui, A., Carvalho, J. C., & Benetti, M. 2016, arXiv e-prints, arXiv:1611.08458 3
- Amenta, N., Bern, M., & Eppstein, D. 1998, *Graph. Models Image Process.*, 60, 125 3
- Anderson, L., Aubourg, E., Bailey, S., et al. 2012, *MNRAS*, 427, 3435 2
- Anderson, L., Aubourg, É., Bailey, S., et al. 2014, *MNRAS*, 441, 24 2
- Bardeen, J. M., Bond, J. R., Kaiser, N., & Szalay, A. S. 1986, *ApJ*, 304, 15 2
- Barrow, J. D., Bhavsar, S. P., & Sonoda, D. H. 1985, *MNRAS*, 216, 17 7
- Beutler, F., Blake, C., Colless, M., et al. 2011, *MNRAS*, 416, 3017 2
- Beutler, F., Blake, C., Colless, M., et al. 2012, *MNRAS*, 423, 3430 2
- Beutler, F., Seo, H.-J., Ross, A. J., et al. 2017, *MNRAS*, 464, 3409 2
- Bolton, A. S., Schlegel, D. J., Aubourg, É., et al. 2012, *Astron. J.*, 144, 144 4
- Bond, J. R., Kofman, L., & Pogosyan, D. 1996, *Nature*, 380, 603 2
- Cao, Y., Gong, Y., Meng, X.-M., et al. 2018, *MNRAS*, 480, 2178 3
- Carvalho, G. C., Bernui, A., Benetti, M., Carvalho, J. C., & Alcaniz, J. S. 2016, *Phys. Rev. D*, 93, 023530 3, 12
- Carvalho, G. C., Bernui, A., Benetti, M., et al. 2020, *Astropart. Phys.*, 119, 102432 3, 12
- Chuang, C.-H., Kitaura, F.-S., Liang, Y., et al. 2017, *Phys. Rev. D*, 95, 063528 2
- Colless, M., Dalton, G., Maddox, S., et al. 2001, *MNRAS*, 328, 1039 2
- Connolly, A. J., Scranton, R., Johnston, D., et al. 2002, *ApJ*, 579, 42 3
- Correa, C. D., & Lindstrom, P. 2013, *Int. J. Uncertainty Quantif.*, 3, 187 7
- Crenshaw, J. F., Leistedt, B., Graham, M. L., et al. 2025, arXiv e-prints, arXiv:2503.06016 3
- Cuillandre, J. C., Bertin, E., Bolzonella, M., et al. 2024, arXiv e-prints, arXiv:2405.13496 3
- Dawson, K. S., Schlegel, D. J., Ahn, C. P., et al. 2013, *Astron. J.*, 145, 10 4
- de Carvalho, E., Bernui, A., Carvalho, G. C., Novaes, C. P., & Xavier, H. S. 2018, *JCAP*, 2018, 064 3
- de Lapparent, V., Geller, M. J., & Huchra, J. P. 1986, *ApJL*, 302, L1 2
- DESI Collaboration, Aghamousa, A., Aguilar, J., et al. 2016, arXiv e-prints, arXiv:1611.00036 3
- DESI Collaboration, Abareshi, B., Aguilar, J., et al. 2022, *Astron. J.*, 164, 207 3
- Ding, J., Li, S., Zheng, Y., et al. 2024, *ApJS*, 270, 25 4, 5, 6
- Edelsbrunner, H., Kirkpatrick, D., & Seidel, R. 1983, *IEEE Trans. Inf. Theory*, 29, 551 3
- Eisenstein, D. J., Annis, J., Gunn, J. E., et al. 2001, *AJ*, 122, 2267 4
- Eisenstein, D. J., Zehavi, I., Hogg, D. W., et al. 2005, *ApJ*, 633, 560 2
- Eisenstein, D. J., Weinberg, D. H., Agol, E., et al. 2011, *AJ*, 142, 72 4

- Euclid Collaboration, Scaramella, R., Amiaux, J., et al. 2022, *A&A*, 662, A112 3
- Euclid Collaboration, Mellier, Y., Abdurro'uf, et al. 2024a, arXiv e-prints, arXiv:2405.13491 3
- Euclid Collaboration, Cropper, M. S., Al-Bahlawan, A., et al. 2024b, arXiv e-prints, arXiv:2405.13492 3
- Euclid Collaboration, Jahnke, K., Gillard, W., et al. 2024c, arXiv e-prints, arXiv:2405.13493 3
- Euclid Collaboration, Duret, V., Escoffier, S., et al. 2025a, arXiv e-prints, arXiv:2503.11621 3
- Euclid Collaboration, Le Brun, V., Bethermin, M., et al. 2025b, arXiv e-prints, arXiv:2503.15308 3
- Fang, F., Forero-Romero, J., Rossi, G., Li, X.-D., & Feng, L.-L. 2019, *MNRAS*, 485, 5276 3
- Feldbrugge, J., van de Weygaert, R., Hidding, J., & Feldbrugge, J. 2018, *J. Cosmol. Astropart. Phys.*, 2018, 027 2
- Forero-Romero, J. E., Contreras, S., & Padilla, N. 2014, *MNRAS*, 443, 1090 2
- Forero-Romero, J. E., Hoffman, Y., Gottlöber, S., Klypin, A., & Yepes, G. 2009, *MNRAS*, 396, 1815 2
- Franco, C., Avila, F., & Bernui, A. 2024, *MNRAS*, 527, 7400 3
- Fu, Z.-S., Qi, Z.-X., Liao, S.-L., et al. 2023, *Front. Astron. Space Sci.*, 10, 1146603 3
- García-Alvarado, M. V., Li, X. D., & Forero-Romero, J. E. 2020, *MNRAS*, 498, L145 3
- Gong, Y., Liu, X., Cao, Y., et al. 2019, *ApJ*, 883, 203 3
- Gott, III, J. R., Jurić, M., Schlegel, D., et al. 2005, *ApJ*, 624, 463 2
- Gu, Y., Yang, X., Han, J., et al. 2024, *MNRAS*, 529, 4015 3
- Guzzo, L., Scodeggio, M., Garilli, B., et al. 2014, *A&A*, 566, A108 2
- Hahn, O., Porciani, C., Carollo, C. M., & Dekel, A. 2007, *MNRAS*, 375, 489 2
- Hoffman, Y., Metuki, O., Yepes, G., et al. 2012, *MNRAS*, 425, 2049 2
- Huchra, J. P., Macri, L. M., Masters, K. L., et al. 2012, *ApJS*, 199, 26 2
- Ivezić, Ž., Kahn, S. M., Tyson, J. A., et al. 2019, *ApJ*, 873, 111 3
- Kirkpatrick, D. G., & Radke, J. D. 1985, in *Machine Intelligence and Pattern Recognition*, Vol. 2, Computational Geometry, ed. G. T. TOUSSAINT (North-Holland), 217 7
- Kitaura, F. S., Yepes, G., & Prada, F. 2014, *Mon. Not. R. Astron. Soc.*, 439, L21 6
- Kitaura, F.-S., Rodríguez-Torres, S., Chuang, C.-H., et al. 2016, *MNRAS*, 456, 4156 4, 6
- Klypin, A., & Holtzman, J. 1997, arXiv e-prints, astro 2
- Knollmann, S. R., & Knebe, A. 2009, *ApJS*, 182, 608 2
- Kumar, D., Mitra, A., Adil, S. A., & Sen, A. A. 2025, *Phys. Rev. D*, 111, 043503 3
- Landy, S. D., & Szalay, A. S. 1993, *ApJ*, 412, 64 11, 12
- Laureijs, R., Amiaux, J., Arduini, S., et al. 2011, arXiv e-prints, arXiv:1110.3193 3
- Li, M., Li, X.-D., Wang, S., & Wang, Y. 2011, *Commun. Theor. Phys.*, 56, 525 18

- LSST Science Collaboration, Abell, P. A., Allison, J., et al. 2009, arXiv e-prints, arXiv:0912.0201 3
- Luo, Z., Li, Y., Lu, J., et al. 2024, MNRAS, 535, 1844 3
- Massara, E., Hahn, C., Eickenberg, M., et al. 2024, arXiv e-prints, arXiv:2404.04228 4
- Matsubara, T., Szalay, A. S., & Pope, A. C. 2004, ApJ, 606, 1 12
- Parkinson, D., Riemer-Sørensen, S., Blake, C., et al. 2012, Phys. Rev. D, 86, 103518 2
- Percival, W. J., Cole, S., Eisenstein, D. J., et al. 2007, MNRAS, 381, 1053 2
- Perlmutter, S., Aldering, G., Goldhaber, G., et al. 1999, ApJ, 517, 565 18
- Planck Collaboration, Ade, P. A. R., Aghanim, N., et al. 2016, A&A, 594, A13 6
- Riess, A. G., Filippenko, A. V., Challis, P., et al. 1998, AJ, 116, 1009 18
- Rodríguez-Torres, S. A., Chuang, C.-H., Prada, F., et al. 2016, MNRAS, 460, 1173 6
- Ross, A. J., Samushia, L., Howlett, C., et al. 2015, MNRAS, 449, 835 2
- Sánchez, A. G., Scóccola, C. G., Ross, A. J., et al. 2012, MNRAS, 425, 415 2
- Sánchez, A. G., Kazin, E. A., Beutler, F., et al. 2013, MNRAS, 433, 1202 2
- Sánchez, A. G., Grieb, J. N., Salazar-Albornoz, S., et al. 2017, MNRAS, 464, 1493 2
- Satpathy, S., A C Croft, R., Ho, S., & Li, B. 2019, MNRAS, 484, 2148 4
- Shi, F., Tian, J., Ding, Z., et al. 2025, Sci. China Phys. Mech. Astron., 68, 249511 3
- Sousbie, T. 2011, MNRAS, 414, 350 2
- Springel, V., White, S. D. M., Tormen, G., & Kauffmann, G. 2001, MNRAS, 328, 726 2
- Storey-Fisher, K., Tinker, J. L., Zhai, Z., et al. 2024, ApJ, 961, 208 4
- Suárez-Pérez, J. F., Camargo, Y., Li, X.-D., & Forero-Romero, J. E. 2021a, ApJ, 922, 204 2
- Suárez-Pérez, J. F., Camargo, Y., Li, X.-D., & Forero-Romero, J. E. 2021b, ApJ, 922, 204 2, 3
- Sui, J., Zou, H., Yang, X., et al. 2025, MNRAS, 538, 395 3
- Tassev, S., Zaldarriaga, M., & Eisenstein, D. J. 2013, JCAP, 2013, 036 4, 5
- Tegmark, M., Blanton, M. R., Strauss, M. A., et al. 2004, ApJ, 606, 702 2
- Venville, B., Parkinson, D., Hurley-Walker, N., Galvin, T. J., & Ross, K. 2024, PASA, 41, e070 3
- Wang, Y., Brunner, R. J., & Dolence, J. C. 2013, MNRAS, 432, 1961 3
- Weinberg, D. H., Mortonson, M. J., Eisenstein, D. J., et al. 2013, Phys. Rep., 530, 87 18
- Weinberg, S. 1989, RMP, 61, 1 18
- White, M. 2016, JCAP, 2016, 057 4
- Wu, Y.-W., & Xia, J.-Q. 2025, ApJ, 979, 3 4
- Xiao, L., Huang, Z., Zheng, Y., Wang, X., & Li, X.-D. 2023, MNRAS, 518, 6253 3
- Xiao, X., Yang, Y., Luo, X., et al. 2022, MNRAS, 513, 595 4

- Xu, T., Cai, Y.-C., Chen, Y., et al. 2025, *ApJ*, 982, 5 4
- Yang, Y., Miao, H., Ma, Q., et al. 2020, *ApJ*, 900, 6 4
- Yin, F., Ding, J., Lai, L., et al. 2024, *Phys. Rev. D*, 109, 123537 1, 3, 6, 9, 10, 17
- Yoo, J., & Watanabe, Y. 2012, *Int. J. Mod. Phys. D*, 21, 1230002 18
- York, D. G., Adelman, J., Anderson, Jr., J. E., et al. 2000, *AJ*, 120, 1579 2
- Zhan, H. 2011, *Sci. Sin. Phys. Mech. Astron.*, 41, 1441 3
- Zhan, H. 2021, *Chinese Science Bulletin*, 66, 1290 3
- Zhang, W., & King, I. 2002, in *Proceedings of the 9th International Conference on Neural Information Processing*, 2002. *ICONIP '02.*, Vol. 3 (IEEE), 1423 3